Normal-state electronic Raman-scattering efficiencies of $YBa_2Cu_3O_{7-\delta}$, $Bi_2Sr_2CaCu_2O_8$, and $Tl_2Ba_2Ca_2Cu_3O_{10}$: Effects of local-density-approximation Fermi-surface mass fluctuations

M.C. Krantz, I.I. Mazin,* and D.H. Leach
Max-Planck-Institut für Festkörperforschung, Heisenbergstrasse 1, D-70569 Stuttgart, Federal Republic of Germany

W.Y. Lee
IBM Almaden Research Center, 650 Harry Road, San Jose, California 95120

M. Cardona
Max-Planck-Institut für Festkörperforschung, Heisenbergstrasse 1, D-70569 Stuttgart, Federal Republic of Germany
(Received 28 June 1994)

Absolute electronic Raman-continuum cross sections have been measured for orthorhombic single-domain Y-123 and Bi-2212 crystals and a tetragonal Tl-2223 film on a MgO substrate ($T_c = 120$ K) in different polarization geometries. They agree well with effective mass fluctuations obtained for Y-123 from Fermi-surface averages of the dispersion calculated from the full-potential linear muffin-tin orbital band structure of Andersen *et al.* The results suggest that anisotropic mass density fluctuations involving various sheets and regions of the Fermi surface are indeed responsible for the electronic Raman continuum and predictable with realistic local-density-approximation band-structure calculations. Decomposition into contributions from the four sheets of the Fermi surface permits separation of interband and intraband mass fluctuations. Anisotropies corresponding to the orthorhombicity and the purely tetragonal A_{1g}, B_{1g}, and B_{2g} symmetries are determined for the three superconductors.

The largely temperature- and frequency-independent electronic Raman-scattering continuum observed in all cuprates,[1–4] as well as in the copperless $Ba_{1-x}K_xBiO_3$ and $Sr_{1-x}La_xTiO_3$ compounds,[5,6] has been studied extensively, and is considered to be an essential part of their unusual normal-state electronic properties and correlation effects. A phenomenological marginal Fermi-liquid theory[7] has been proposed, as well as some microscopic models, like the nested Fermi liquid,[8] the electron-phonon strong-coupling model,[9] and the collision-limited scattering of light by mass-density fluctuations.[10] The effects of strong inelastic scattering and interband transitions have also been considered.[11] Aside from the origin of the frequency-independent behavior, the relative strength of the continua observed in different polarizations is an important fact to be compared with theory. In metals this quantity is mainly determined by the Raman vertex for electronic scattering, which is given by the effective mass tensor contracted with the incident and scattered polarization vectors. The microscopic scattering mechanisms which lead to electronic Raman-scattering have been extensively studied in doped semiconductors (see Ref. 12 and reviews in Refs. 13–15). Common to all mechanisms are density fluctuations on different parts of the Fermi surface with a multicomponent plasma producing variations of zero net charge but a net coupling to the scattering Hamiltonian since the sum of the scattering vertices does not cancel. In a metal only charge fluctuations which carry zero net charge are observable, because charge-carrying fluctuations are screened out. In the case of a single-sheeted Fermi surface the chargeless fluctuations must involve Fermi-surface harmonics with $L > 0$.[16] Nonzero charge fluctuations corresponding to $L = 0$ symmetry can also be obtained in the case of multisheeted Fermi surfaces.[17] Here L denotes Allen's Fermi surface harmonics,[16] not $\{l, m\}$ of the angular harmonics. For instance, in the case of n-sheeted Fermi surfaces $L = 0$ corresponds to a function constant on all sheets, while $L = 1, \ldots, n-1$ harmonics are linear combinations of constants on each sheet, different for different sheets and carrying no net charge.

In order to obtain a better understanding of the electronic Raman-scattering vertex and its microscopic origin we have measured absolute Raman cross sections of the electronic continuum of Y-123, Bi-2212, and Tl-2223 at room temperature in different polarizations and compared them to mass fluctuations, calculated for Y-123 from the local-density-functional (LDA) full-potential linear-muffin-tin-orbital (LMTO) band structure of Anderson *et al.*[18] The high accuracy of the band structure is important for the calculation of mass tensors and their anisotropies in k space.

Figures 1–3 display the spectra for a Y-123 single-domain crystal, a Bi-2212 single crystal, and a Tl-2223 epitaxial film taken in several polarization geometries at 300 K. The results were confirmed with multiple measurements on different spots of the samples. The polarization geometries are denoted according to the crystal

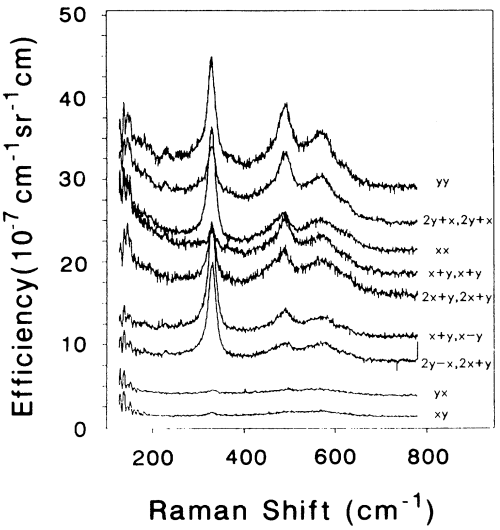

FIG. 1. 300 K Raman spectra of a $YBa_2Cu_3O_{7-\delta}$ single-domain crystal taken with nine different polarizations in the a-b plane at $\lambda_L = 514$ nm ($T = 300$ K). The spectra are displayed in absolute units but include consecutive offsets of (0,1,2, ..., 8) × 2.5. The electronic Raman cross sections were determined at a 700 cm^{-1} frequency shift.

axes, i.e., $x \parallel a$ and $y \parallel b$, with a, b being parallel to the CuO bonds in Y-123 and Tl-2223 and at 45° in Bi-2212. The absolute Raman-scattering efficiencies were determined by comparison with the known cross section of BaF_2, whereby the optical constants of the superconductors and BaF_2, and also the instrument response, were taken into account.[19] The absolute electronic Raman-scattering efficiencies, shown in Table I, were determined at high-frequency shifts where they are not affected by phonons.

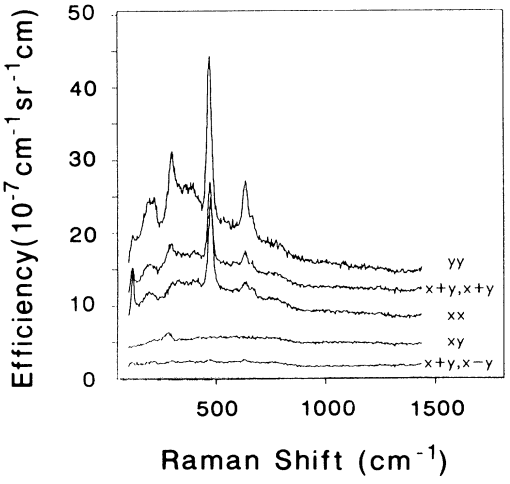

FIG. 2. Raman spectra of a $Bi_2Sr_2CaCu_2O_8$ single crystal taken in different polarization geometries at $\lambda_L = 488$ nm ($T = 300$ K). The data are displayed in absolute units with consecutive offsets of (0,1,2, ... , 4) × 2.5. The electronic Raman cross sections were determined at 1200 cm^{-1}.

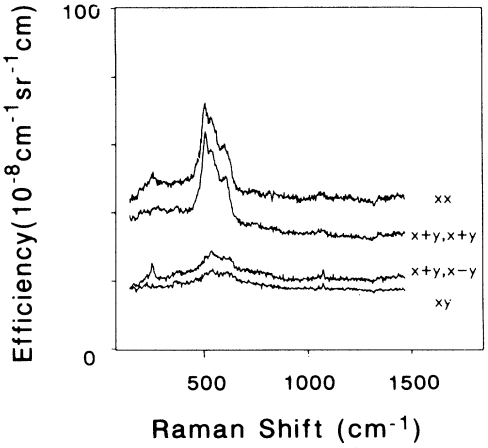

FIG. 3. Raman spectra of a $Tl_2Ba_2Ca_2Cu_3O_{10}$ epitaxial film on a MgO substrate, $T_c = 120$ K ($\lambda_L = 488$ nm, $T = 300$ K) displayed in absolute units. The electronic Raman cross sections were determined at 1200 cm^{-1}.

The orthorhombicity is produced in Bi-2212 [approximate space group $Fmmm$ (D_{2h}^{23})] by a strong incommensurate [010] modulation and in Y-123 [space group $Pmmm$ (D_{2h}^{1})] by linear chains also along [010]. Tl-2223 is close to ideally tetragonal [space group $I4/mmm$ (D_{4h}^{17})]. In the tetragonal case the xx and yy scattering configurations yield equal scattered intensities which correspond to excitations of A_{1g} (x^2+y^2) plus B_{1g} (x^2-y^2) symmetry (D_{4h} point group) while the xy configuration corresponds to excitations of B_{2g} symmetry. Hence, three independent parameters are needed to represent scattering with in-plane polarizations. We chose these parameters in the form of Raman-tensor elements

TABLE I. Absolute polarization-dependent Raman efficiencies for electronic scattering in Y-123 ($\lambda_L = 514$ nm, $\omega = 700$ cm^{-1}), Bi-2212 ($\lambda_L = 488$ nm, $\omega = 1200$ cm^{-1}), and Tl-2223 ($\lambda_L = 488$ nm, $\omega = 1200$ cm^{-1}) in units of (10^{-8} cm^{-1} sr^{-1} cm). The data (accuracy ± 30%) include corrections for optical constants. Fits to these data yield Raman tensors (assumed to be real) in units of (10^{-4} cm$^{-1/2}$ sr$^{-1/2}$ cm$^{1/2}$) for tetragonal A_{1g}, B_{1g}, and B_{2g} symmetry and orthorhombicity, i.e., $\begin{pmatrix} a & \\ & a \end{pmatrix}$, $\begin{pmatrix} b & \\ & -b \end{pmatrix}$, $\begin{pmatrix} c & \\ & c \end{pmatrix}$, $\begin{pmatrix} 0 & e \\ e & \end{pmatrix}$. Additional Y-123 data (Fig. 1) are included in the fits but not listed.

Polarization	Y-123		Bi-2212		Tl-2223	
e_L e_S	Data	Fit	Data	Fit	Data	Fit
yy	27	28	12	12	14	13
$x+y, x+y$	17	17	11	11	10	11
xx	14	15	9.0	8.8	14	13
$x+y, x-y$	9.0	8.5	3.5	4.0	6.1	6.8
xy	3.4	3.9	5.3	4.8	5.4	4.7
A_{1g}	$a = 3.1$		$a = 2.4$		$a = 2.5$	
B_{1g}	$b = 2.3$		$b = 1.8$		$b = 2.6$	
B_{2g}	$c = 2.0$		$c = 2.2$		$c = 2.2$	
Orthorhombicity	$e = 3.6$		$e = 1.8$		$e = 0.06$	

$$A_{1g}\begin{pmatrix} a & \\ & a \end{pmatrix} \quad B_{1g}\begin{pmatrix} b & \\ & -b \end{pmatrix} \quad B_{2g}\begin{pmatrix} & c \\ c & \end{pmatrix} . \quad (1)$$

If the crystal is orthorhombic (D_{2h} point group), the Raman-tensor B_{1g} of Eq. (1) lowers its symmetry to A_{1g} while the B_{2g} symmetry must be labeled B_{1g}. The existence of two Raman tensors of A_{1g} symmetry demands the introduction of an extra parameter to represent the scattered intensities for in-plane polarizations which become proportional to averages of the squares of each one of the A_{1g}-tensor component and also of their cross product. We introduce this additional parameter in a form which has a clear physical significance: the contribution of the strongly asymmetric chains with only m_{yy} nonvanishing masses. This can be represented by an additional Raman-tensor

$$\begin{pmatrix} 0 & \\ & e \end{pmatrix} . \quad (2)$$

In order to permit a comparison between the compounds of orthorhombic and tetragonal symmetry we have extracted the orthorhombic contribution, i.e., $I_{yy} - I_{xx}$, in Y-123 and Bi-2212, together with the scattering intensities which can be attributed to purely tetragonal Raman-tensor elements of A_{1g}, B_{1g}, and B_{2g} symmetry for all materials. The measured polarization-dependent intensities yield the fitted values for tensor elements contained in Table I. They represent all measured intensities with an error of less than 20%, thus justifying the reduction performed above in terms of only *symmetric* Raman-tensors. Note that for Tl-2223 the orthorhombic term $e \simeq 0.06$ is negligible, as expected for a tetragonal compound. In the presence of electronic resonances with either incident or the scattered polarizations *antisymmetric* Raman-tensor components are possible. In view of the fact that there is one more experimental data than adjustable parameters, the level of agreement between measured and fitted intensities indicates that effects of antisymmetric tensors are not pronounced and we neglect them in the context of this paper. Absolute cross sections predicted under the assumption of k conservation are lower than the observed ones by about one order of magnitude.[13] This discrepancy is lifted in the non-k-conserving collision-limited regime.[10,13,20] Thus, due to the strong scattering cross section observed in Y-123 (Table I) only the latter, i.e., the collision-limited case, will be considered here.

In the collision-limited regime the Raman-scattering efficiency is given by[20]

$$\frac{d^2S}{d\omega d\Omega} = [1 + n(\omega, T)] \frac{\omega \Gamma B}{\omega^2 + \Gamma^2}, \quad (3)$$

with Γ representing the scattering rate and

$$B = \frac{e^4}{\hbar \pi c^4} N(\varepsilon_F) \left\langle \left| \mathbf{e}_L \cdot \left(\frac{\partial^2 \varepsilon_{\mathbf{k}\alpha}}{\partial \mathbf{k} \partial \mathbf{k}} - \left\langle \frac{\partial^2 \varepsilon_{\mathbf{k}\alpha}}{\partial \mathbf{k} \partial \mathbf{k}} \right\rangle \right) \cdot \mathbf{e}_S \right|^2 \right\rangle . \quad (4)$$

Here ε_{k_α} is the energy of the electron in band α with momentum $\hbar k$ and $N(\varepsilon_F)$, the density of states at the Fermi level per unit volume and unit energy. The brackets $\langle\ \rangle$ denote the Fermi surface average, $\langle f_{\mathbf{k}} \rangle \equiv \sum_{\mathbf{k}_\alpha} f_{\mathbf{k}} \delta(\varepsilon_F - \varepsilon_{\mathbf{k}_\alpha}) / \sum_{\mathbf{k}_\alpha} \delta(\varepsilon_F - \varepsilon_{\mathbf{k}_\alpha})$. Equation (4) can be also rewritten in a more illustrative form

$$B = \frac{\hbar e^4}{\pi c^4} N(\varepsilon_F) \left\langle \left| \mathbf{e}_L \cdot \left(\overleftrightarrow{m}^{-1} - \left\langle \overleftrightarrow{m}^{-1} \right\rangle \right) \cdot \mathbf{e}_S \right|^2 \right\rangle ; \quad (5)$$

where

$$\left\langle \left| \mathbf{e}_L \cdot \left(\overleftrightarrow{m}^{-1} - \left\langle \overleftrightarrow{m}^{-1} \right\rangle \right) \cdot \mathbf{e}_S \right|^2 \right\rangle = \left\langle \left| \mathbf{e}_L \overleftrightarrow{m}^{-1} \mathbf{e}_S \right|^2 \right\rangle - \left\langle \left| \mathbf{e}_L \overleftrightarrow{m}^{-1} \mathbf{e}_S \right| \right\rangle^2 ; \quad (6)$$

i.e., the observable unscreened mass fluctuations are the difference between the bare and the screened-out ones (the latter are labeled as *screened* in Tables II and III).

A widely used but possibly not unique way to explain the frequency independence of the Raman efficiency, known as marginal fermi-liquid (MFL) theory, is to introduce a linear dependence of the relaxation rate on the frequency ω. The microscopic origin of MFL behavior is not clear yet. Some associate it with electron-phonon interaction[11] while others relate it to peculiarities of the electronic structure.[8] We do not discuss this topic here and refer the interested reader to the vast literature on MFL theory.[7] In our calculations we used the above expression with $\Gamma = 0.5\omega$, which is consistent also with the large electron-energy-loss-spectroscopy (EELS) damping width.[22] We should note at this point that Eqs. (4) and (5) are derived within $k \cdot p$ perturbation theory provided ω_S and ω_L are away from strong interband optical transitions. The latter is not true for the usual experimental conditions. Nevertheless, calculations in Ref. 11 at two ω_L's (1.9 and 2.7 eV) show that the effect of the resonance-enhancement factors by which Eqs. (4) and (5) have to be corrected is approximately the same for all scattering configurations. We shall come back to this point later.

The electronic mass tensor of $YBa_2Cu_3O_{7-\delta}$ was calculated from the full-potential LMTO-LDA band structure[18] by linear tetrahedron interpolation of the second derivative of the energy bands computed by direct numerical differentiation of the electronic energies at a $\mathbf{k}$ mesh of 845 inequivalent points. The absolute accuracy for the Fermi-surface average in Eq. (4) was estimated by the fulfillment of symmetry relations to be better than $0.04\left(\frac{1}{m_e}\right)^2$, which corresponds for different components to (3–10)% relative accuracy. Using these results the bare, screened-out, and unscreened mass fluctuations in each scattering configuration and corresponding cross sections were calculated. They are presented in Table II.

The agreement between the normalized data and the *ab initio* calculated relative intensities is good. The yy-xx and yy-$(x+y, x+y)$ anisotropies are reproduced well. The ratios between calculated and measured $x+y, x-y$, and xy intensities are similar even though the relative in-

TABLE II. Calculated electronic Raman efficiencies in the collision-limited regime [Eq. (3)] (Ref. 21) produced from the Fermi-surface averages of the masses from LDA full-potential calculations for $YBa_2Cu_3O_7$. Bare, screened, and unscreened mass fluctuation results are given in the yy, $x+y, x+y$, xx, $x+y, x-y$, and xy polarizations. The units are (10^{-8} cm^{-1} sr^{-1} cm). The unscreened predictions and data have been normalized to their yy values to facilitate comparison with experimental ratios.

	Calculations				Experiment	
Polarization geometry	Bare $\left\langle \left(e_L \frac{m_0}{m^*} e_S\right)^2 \right\rangle$	Screened $\left(\left\langle e_L \frac{m_0}{m^*} e_S \right\rangle^2\right)$	Unscreened $\left\langle \left(e_L \left(\frac{m_0}{m^*} - \left\langle \frac{m_0}{m^*} \right\rangle\right) e_S\right)^2 \right\rangle$	Unscreened normalized	Normalized data	Data
yy	6.9	1.1	5.8	1	1	27
$x+y, x+y$	4.0	0.64	3.4	0.59	0.63	17
xx	3.9	0.31	3.6	0.62	0.52	14
$x+y, x-y$	3.0	0.05	2.9	0.50	0.33	9.0
xy	1.6	0	1.6	0.27	0.13	3.4

tensities of both crossed polarizations are somewhat low. The effect of screening, which is expected to be present in the parallel and absent in the xy crossed polarizations (and very small in $x+y, x-y$), is reproduced well by the calculation. The screened-out components (A_{1g} symmetry), which correspond to the electron-density fluctuations carrying net charge, are small compared to the remaining unscreened density fluctuations of zero net charge. This may arise from the strong angular dependence of the electronic mass or the strong difference of the masses in different bands (involving most likely positive as well as negative masses). We thus performed the calculations for the four sheets *separately*, with the results given in Table III. The hybridized chain band [Cu(1) $d_{z^2-y^2}$ O(1) p_y] and antibonding plane bands [Cu(2) $d_{x^2-y^2}$ O(2) p_x O(3) p_y] were relabeled at the crossover points so as the preserve their dominant plane or chain character. Intraband screened components are given for each band and polarization. These single-sheet fluctuations would be screened, as indicated, if there were no other bands in the system. An investigation of Table III yields the following: Intraband mass fluctuations for the chain band are almost completely screened as expected for a nearly one-dimensional band. Mass fluctuations from the antibonding plane band dominate over the ones from all other bands, which is understandable due to the strong dimpling of the corresponding Fermi surface[18] leading to small average mass and in view of the strong extended Van Hove singularities present in this band near the Fermi level also partially reflected in the density of states. As opposed to the antibonding sheet the largely flat pieces of the bonding Fermi surface, and the nearly linear (i.e., zero second derivative) dispersion in directions perpendicular to these flat portions,[18] lead to small inverse mass fluctuations of this band. For yy polarizations intraband screening of the bare mass fluctuations amounts to about 50%, whereas only about 15% of the bare total is screened out. This suggests that about 45% of the observed unscreened scattering originates from interband mass fluctuations for this polarization configuration. Similarly for the other polarizations the fractions of intraband screening, unscreened total, and unscreened interband scattering are for (xx), 31%, 8%, 25%; for ($x+y, x+y$), 45%, 16%, 35%; and for ($x+y, x-y$), 21%, 2%, 22%, respectively. Thus, interband mass fluctuations are significant but not solely responsible for the xx-yy anisotropy. For ($x+y, x-y$) polarization intraband screening is only non-negligible in the chain band, consistent with its strong orthorhombicity. Investigating Table I the orthorhombicity in the electronic Raman intensities is found to be about twice as large in Y-123 as in Bi-2212. The A_{1g} intensities decrease while the B_{1g} and B_{2g} intensities increase from Y-123 to Tl-2223. If the B_{1g} and B_{2g} intensities in Bi-2212 are exchanged (i.e., equiv-

TABLE III. Mass fluctuations produced from individual sheets of the $YBa_2Cu_3O_7$ Fermi surface (i.e., intraband) in comparison to the total fluctuations produced from the whole multisheeted surface (i.e., intraband + interband) in units of $\left(\frac{1}{m_e}\right)^2$. The individual mass fluctuations have been multiplied by their partial contribution to the total density of states at the Fermi surface (70 states/unit cell/Hartree including both spins), i.e., chains, $\frac{11}{70} = 0.16$; antibonding planes, $\frac{29}{70} = 0.41$; bonding planes, $\frac{12}{70} = 0.17$; and apical oxygen, $\frac{18}{70} = 0.26$. The hybridized chain and antibonding plane sheets have been separated and relabeled at the crossover points. Results for bare and screened-out individual intra- and total intra- and interband mass fluctuations are given. Interband mass fluctuations are derivable by subtracting the sum of the unscreened individual from the unscreened total results.

Polarization	Chain		Antibonding planes		Bonding planes		Apical oxygen		Total	
	Bare	Screened	Bare	Screened	Bare	Screened	Bare	Screened	Bare	Screened
yy	0.79	0.62	0.88	0.29	0.06	0	0.10	0.07	1.82	0.28
$x+y, x+y$	0.25	0.15	0.47	0.25	0.20	0.01	0.14	0.05	1.06	0.17
xx	0.02	0	0.66	0.23	0.29	0.05	0.06	0.04	1.03	0.08
$x+y, x-y$	0.20	0.16	0.46	0	0.10	0.01	0.02	0	0.78	0.01
xy	0.05	0	0.16	0	0.13	0	0.08	0	0.42	0

alent to redefining the a and b axes along Cu-O bonds as in Y-123 and Tl-2223), the B_{1g} and B_{2g} Raman-tensors increase continuously.

These effects can be understood qualitatively from the shapes of the Fermi surfaces of Y-123, Bi-2212,[23] and Tl-2223.[24] Similar to Y-123 the Fermi surface of Bi-2212 displays two closely spaced flat and dimpled sheets originating from the bonding and antibonding O p_x Cu $d_{x^2-y^2}$ O p_y bands. The smaller orthorhombicity in Bi-2212 (as measured by Raman scattering) as well as the overall smaller A_{1g} intensity can be attributed to the absence of the chain band and of the corresponding intra- and interband mass fluctuations predicted for Y-123. In Tl-2223 there are three closely spaced CuO_2-plane Fermi-surface sheets.[24,25] They suggest the presence of very similar and more isotropic masses than in the case of $YBa_2Cu_3O_7$. Thus, the small A_{1g} intensity in spite of the third CuO_2-plane Fermi-surface sheet can be understood as resulting from stronger interband screening of the A_{1g} mass fluctuations than in Bi-2212 while the higher intensities in B_{1g} and B_{2g} symmetry, where no screening is present, can be attributed to the additional band.

The absolute cross sections measured for the electronic Raman spectra of Y-123 are about four times larger than the ones calculated from the band structure (Tables I and II). This can possibly result from an interband excitation resonance involving the proximity of bands approximately $\pm\hbar\omega_{\text{laser}}$ away from the Fermi energy. The measured anistropies do not seem to be affected by resonances, a fact which is already suggested by the calculations of Ref. 11 (see also the measurements in Ref. 4) for $\hbar\omega = 1.9$ and 2.7 eV excitation. The broad nature of the intermediate-state resonances may help to reduce resonant-anisotropy effects, as borne out in an orthorhombic crystal by the near equality of the xy and yx electronic Raman cross sections in Y-123 which differ by less than 15%, well within the range of experimental error. In addition to resonance effects reduced masses resulting from correlation effects, as implied by the marginal Fermi-liquid phenomenology,[7] would also enhance the Raman cross section. In view of the fact that absolute cross section determinations, when we consider all sources of error, may be off by a factor of 2, a discrepancy between the nonresonant theory and experiment by a factor of 4 is not to be regarded as serious. The overall agreement of the calculated mass fluctuation averages around the Fermi surface with the measured anisotropy of the electronic scattering continua for all polarization geometries and the correct prediction of screening effects suggest that the electronic Raman continua are indeed produced by electronic mass-density fluctuations. These fluctuations are of intraband as well as interband nature.[26] The important implications of the interband fluctuations for scattering in the superconducting state have been discussed recently.[17]

In summary, we have measured absolute Raman cross sections of the electronic continua in Y-123, Bi-2212, and Tl-2223 and compared the Y-123 results to the corresponding unscreened mass fluctuations at the Fermi surface calculated from the LMTO full-potential band structure. The relative scattering cross sections for various polarizations agree well with the calculation, suggesting that the Raman continuum arises from density fluctuations of conduction electrons. The absolute Raman intensities are reproduced by the calculation in the collision-limited regime especially if some enhancement due to resonance of either the laser or the scattered frequency with electronic interband transitions is taken into account.

We would like to thank C. Kendziora for making available the $Bi_2Sr_2CaCa_2O_8$ crystal used in this work.

* Present address: Geophysical Laboratory, Carnegie Institution of Washington, 5251 Broad Branch Rd., Washington, D.C.

[1] T. Staufer, R. Hackl, and P. Müller, Solid State Commun. **75**, 975 (1990).
[2] M.C. Krantz, H.J. Rosen, J.Y.T. Wei, and D.E. Morris, Phys. Rev. B **40**, 2635 (1989); M.C. Krantz, J. Phys. Chem. Solids **54**, 1331 (1993).
[3] F. Slakey, M.V. Klein, J.P. Rice, and D.M. Ginsberg, Phys. Rev. B **43**, 3764 (1991).
[4] D. Resnik, M.V. Klein, W.C. Lee, D.M. Ginsberg, and S.W. Cheng, Phys. Rev. B **46**, 11725 (1992).
[5] S. Sugai, Y. Enamoto, and T. Murakami, Solid State Commun. **72**, 1193 (1989).
[6] T. Katsufuji and Y. Tokura, Phys. Rev. B **49**, 4372 (1994).
[7] C.M. Varma, P.B. Littlewood, S. Schmidt-Rink, E. Abrahams, and A.E. Ruckenstein, Phys. Rev. Lett. **63**, 1996 (1989).
[8] A. Virosztek and J. Ruvalds, Phys. Rev. Lett. **67**, 1657 (1991).
[9] V.N. Kostur and G.M. Eliasberg, JETP Lett. **53**, 391 (1991).
[10] A. Zawadovski and M. Cardona, Phys. Rev. B **42**, 10732 (1990).
[11] S.N. Rashkeev and G. Wendin, Phys. Rev. B **47**, 11603 (1993); Z. Phys. B **93**, 33 (1993).
[12] M. Chandrasekhar, M. Cardona, and E.O. Kane, Phys. Rev. B **16**, 3579 (1977); M. Chandrasekhar, U. Rössler, and M. Cardona, *ibid.* **22**, 761 (1980).
[13] M. Cardona and I.P. Ipatova, in *Elementary Excitations in Solids*, edited by J.L. Birman, C. Sebenne, and R.F. Wallis (Elsevier, Amsterdam, 1992), p. 237.
[14] B.H. Bairamov, I.P. Ipatova, and V.A. Voitenko, Phys. Rep. **229**, 221 (1993).
[15] G. Abstreiter, M. Cardona, and A. Pinczuk, in *Light Scattering in Solids IV*, edited by M. Cardona and G. Güntherodt (Springer, Berlin, 1984), Chap. 1.
[16] P.B. Allen, Phys. Rev. B **13**, 1416 (1976); **17**, 3725 (1978). The Fermi-surface harmonics are taken to be orthonormal on the complete Fermi surface.
[17] M.C. Krantz and M. Cardona, Phys. Rev. Lett. **72**, 3290 (1994).
[18] O.K. Andersen, A.I. Lichtenstein, C.O. Rodriguez, I.I. Mazin, O. Jepsen, V.P. Antropov, O. Gunnarson, and S. Gopalan, Physica C **185-189**, 147 (1991).
[19] J.M. Calleja, H. Vogt, and M. Cardona, Philos. Mag. A **45**, 239 (1982). In the case of Y-123, the absolute efficiency was also estimated by comparison with that of the phonons

given by E.T. Heyen *et al.*, Phys. Rev. Lett. **65**, 3048 (1990). The optical constants of J. Kircher *et al.*, Phys. Rev. B **44**, 217 (1991); M. Garriga *et al.*, J. Opt. Soc. Am. **6**, 470 (1989); and Tl-2212 for Tl-2223 (i.e., $\varepsilon_1 = 4.2$, $\varepsilon_2 = 2.0$) were used.

[20] I.P. Ipatova, A.V. Subashiev, and V.A. Voitenko, Solid State Commun. **37**, 893 (1981).

[21] A coefficient of 0.4 was used for $(1 + n)\omega\Gamma/(\omega^2 + \Gamma^2)$ in (3) consistent with the frequency- and temperature-independent continua produced by $\Gamma = \sqrt{(\alpha\omega)^2 - (\beta T)^2}$ and the marginal Fermi-liquid phenomenology.

[22] EELS probes the spectrum of plasmons, i.e., of longitudinal charge-density fluctuations. Physically, it is similar to the electronic Raman-scattering also probing longitudinal excitations; hence it makes sense in the context of light scattering by intraband electronic excitations to refer to the EELS relaxation frequency.

[23] S. Massida, J. Yu, and A.J. Freeman, Physica C **152**, 251 (1988).

[24] V.V. Tatarskii and M. Paranthaman, Phys. Rev. B **47**, 14489 (1993).

[25] R.V. Kasowski, W.Y. Hsu, and A.M. Herrman, Phys. Rev. B **38**, 6470 (1988).

[26] Of course there are, in principle, other potential sources of the anisotropy (both angular and interband) of the scattering rate (see Ref. 10); however, these effects are very hard to estimate. In view of the strong correlation with the mass anisotropy observed here we believe that these effects are not important. In particular, one can expect the scattering rate to be relatively isotropic. Similarly for the transport relaxation rate, which appears to be nearly isotropic, all transport anisotropy again is due to the anisotropy of the Fermi surface [see I.I. Mazin and O.V. Dolgov, Phys. Rev. B **45**, 2509 (1992)].